Geophysical Journal International

*Geophys. J. Int.* (2012) **191,** 591–600 doi: 10.1111/j.1365-246X.2012.05603.x

# An iterative algorithm for separation of *S* and *ScS* waves of great earthquakes

Zhulin Yu,[1] Sidao Ni,[2] Shengji Wei,[3] Xiangfang Zeng,[1] Wenbo Wu[1] and Zhiwei Li[2]

[1] *Mengcheng National Geophysical Observatory, University of Science and Technology of China, Hefei, Anhui, China. E-mail: sdni@whigg.ac.cn*
[2] *State Key Laboratory of Geodesy and Earth's Dynamics, CAS Institute of Geodesy and Geophysics, Wuhan, Hubei, China*
[3] *Seismological Laboratory, Division of Geological and Planetary Sciences, California Institute of Technology, Pasadena, CA* 91125*, USA*

Accepted 2012 July 2. Received 2012 July 2; in original form 2011 December 28

## SUMMARY

Teleseismic *SH* waves are essential for imaging the rupture processes of large earthquakes. However, for great earthquakes (*M*8+) such as the 2004 Sumatra earthquake, the 2008 Wenchuan earthquake and the recent Tohoku-Oki earthquake, the source duration is very long (>100 s). Thus the direct *SH* waves are overlapped with *ScS* waves for epicentral distances larger than 60°, leaving contaminated *S* waves for source processes modelling. Therefore artefacts in finite fault models of large earthquake could be produced with such contaminated body waves. We propose an iterative algorithm based on the slowness information of *S* and *ScS* waves and stacking technique, to separate *S* and *ScS* waves with records from a regional seismic network. Tests on various synthetic data sets show that the algorithm is effective in retrieving teleseismic *SH* waveforms from complicated wave trains containing both *S* and *ScS*. Separation of waveforms for the 2008 Wenchuan earthquake with our algorithm clearly demonstrates the influence of *ScS* energy, suggesting necessity of recovering *S* waves.

**Key words:** Time series analysis; Earthquake dynamics; Earthquake source observations; Body waves.



## INTRODUCTION

In the past decade, a few great earthquakes with duration about 100 s or longer occurred near plate boundaries or in the interior of continents, and regrettably caused huge property damage and loss of human lives. For example, the 2004 Sumatra earthquake lasted about 500 s (Ammon *et al.* 2005; Ni *et al.* 2005), while the rupture duration of the 2008 Wenchuan earthquake and the recent $M_w$ 9.0 Tohoku-Oki earthquake is around 110 and 150 s, respectively (Xu *et al.* 2009; Ammon *et al.* 2011; Simons *et al.* 2011). For those strong earthquakes, accurate models of rupture processes are fundamental for understanding the seismogenic mechanisms, rupture dynamics and strong motion simulation. Finite-fault inversion has been widely accepted to resolve rupture processes, and it was applied as early as in the 1970s (Olson & Apsel 1982; Hartzell & Heaton 1983). After decades of intensive research, various inversion methods have been proposed to improve accuracy of finite fault models with single data set or jointly with multiple data sets. For example, strong ground motion (Olson & Apsel 1982; Fukuyama & Mikumo 1993; Pino *et al.* 1999; Zhang *et al.* 2008), teleseismic body wave records (Kikuchi & Kanamori 1982; Mendoza & Hartzell 1988; Das & Kostrov 1990; Ammon *et al.* 2005), high-rate GPS recordings (Ammon *et al.* 2011), and InSAR data (Peltzer & Rosen 1995; Shen *et al.* 2009) have been exploited in finite fault source inversion either alone or jointly.

Among the above methods, inversion with teleseismic body waves has advantages in the following aspects. First, almost any global large earthquakes can be recorded with good azimuth and distance coverage for the current GSN/IRIS network, unlike the strong motion data, or GPS/INSAR data, which is only available for limited geographic regions such as California or Japan. Moreover, teleseismic *P* or *SH* wave data can be retrieved within dozens of minutes after the earthquake, thus enabling rapid source inversion. Secondly, teleseismic body waves contain temporal information of the rupture processes, unlike static geodetic data sets.

However, there are also complexities associated with teleseismic body waveform data, which may cause artefacts in finite fault models. Usually only *P* waves or *SH* waves for distances between 30° and 90° are included for teleseimic waveform inversion to avoid complexities due to upper mantle triplication or diffraction along the core–mantle boundary (CMB, Kikuchi & Kanamori 1982; Ji *et al.* 2002; Antolik *et al.* 2006). However, the core reflected waves such as *PcP* or *ScS* are typically not taken into account in these studies. Given the relatively weak amplitude, *PcP* may play insignificant roles in *P* wave trains. But *ScS* is expected to be strong because of the total reflection from CMB as no shear waves can propagate in the fluid outer core. Thus *ScS* could complicate teleseismic *S* waveforms, especially at large distances where the time interval between *S* and *ScS* is small. For large earthquakes of very long duration, other secondary body waves such as *PP* may also interfere with *P* waves.

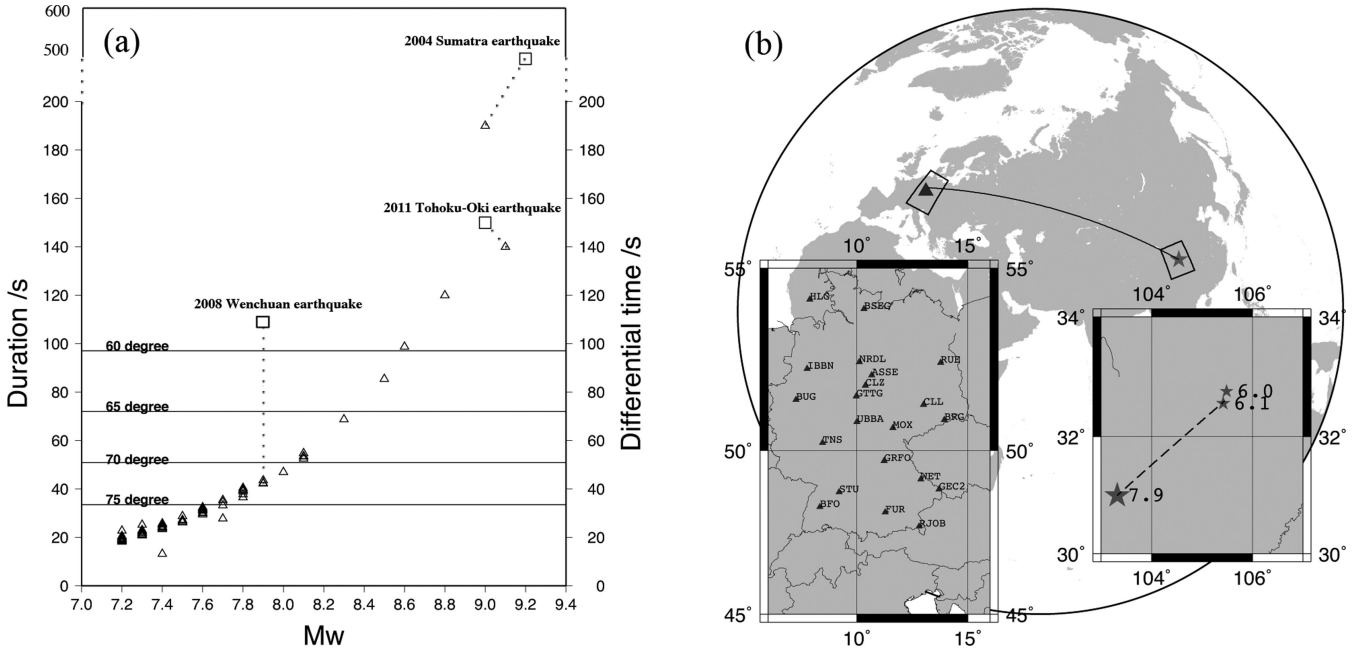


**Figure 1.** (a) Comparison between source duration (left vertical axis) and moment magnitude ($M_w$). Source duration (triangles) and $M_w$ are from Global CMT. For the Wenchuan earthquake, the Tohuku-Oki earthquake and the Great Sumatra earthquake, more accurate estimate of source durations are indicated with squares. The solid lines stand for the theoretical *ScS*-*S* differential time at distances of 60°, 65°, 70°, 75°. (b) The 2008 Wenchuan earthquake, its aftershocks (stars) and seismic stations in GRSN (triangles). The distance between the events and stations is about 70°.

Nonetheless, previous source inversions with teleseismic waveform usually ignore the above secondary phases for short-duration earthquakes since they may arrive too late to interfere with *P* or *S* phases. As the inversion relies on the mismatch between synthetic and observed seismograms (Ji *et al.* 2002), it is essential to understand the seismic phase components in the teleseismic waveform data.

To demonstrate the relevance of *ScS* in complicating *SH* waveforms, in Fig. 1(a) we compare the differential traveltime between *S* and *ScS* to the source duration of earthquakes versus moment magnitude as expected from the scaling laws (Kanamori & Anderson 1975; Houston 2001) or as reported by Global CMT. We only list earthquakes larger than $M_w$ 7.2 since 2004, and the moment magnitude is from Global CMT. Obviously the source duration of the 2008 Wenchuan earthquake and the 2004 Sumatra earthquake are underestimated as compared with detailed waveform studies, which should be around 110 and 500 s, respectively (Ni *et al.* 2005; Ammon *et al.* 2005; Ishii *et al.* 2005; Kruger *et al.* 2005; Xu *et al.* 2009). If we assume that the scaling law works accurately, it suggests that *S* and *ScS* at epicentral distances larger than 75° will have differential traveltime shorter than the duration of $M_w$ 7.7+ earthquakes. And for $M_w$8.3+ earthquakes, *SH* waveform data for distances larger than 65° is expected to be contaminated by *ScS*. However, the scaling law only works approximately and may depend on tectonic settings. In the case of the $M_w$ 7.9 Wenchuan earthquake, the source duration is about 110 s, *SH* waveform data could be interfered with *ScS* even for distances as close as 60°. In such cases, artefacts in finite fault models may emerge if the waveforms contaminated by *ScS* are assumed to contain *S* wave only. Therefore, an algorithm for separating *S* and *ScS* would be helpful for accurate finite fault source inversions.

In previous studies, linear stacking is widely used to enhance target seismic phases in waveform data (Avants *et al.* 2006), and reasonable results can be achieved when the number of stations is sufficiently large. But when it is not, the target phase still suffers substantially from interference of other signals. On the other hand, eigenimage processing is demonstrated to be useful in isolating the secondary phases from major components (Rondenay & Fischer 2003). In this paper, we propose a new algorithm for separating *S* and *ScS* based on iterative procedure as detailed in the following section. Then we apply the algorithm to waveform data recorded on the German Regional Seismic Network (GRSN) for the Wenchuan earthquake and its two aftershocks in Section 'Applications' (Fig. 1b), and demonstrate that about four traces of waveform data are needed to recover *S* wave. And in the discussion and conclusion section, we propose that the algorithm is applicable for the current station coverage with GSN and some regional seismic networks.

## METHODOLOGY

*ScS* phase is typically a strong phase following *S* phase on the tangential component because *SH* waves should be totally reflected from the CMB. For distances larger than 60°, *SS* waves arrive much later than *S* wave. Therefore, it is reasonable to assume that only *S* and *ScS* phases dominate the typical time window starting from *S* as used in most source inversion studies. Then, the seismic signals recorded on a number of stations can be approximated as:

$$X_k(t) = S_S(t) + S_{ScS}(t - \Delta T_k) + Q_k(t). \quad (1)$$

In eq. (1), $k$ stands for the station number, in the range from 1 to $N$, and $N$ is the total number of stations. $Q_k(t)$ is microseismic noise or scattered waves. $S_s(t)$ and $S_{ScS}(t)$ are the *S* and *ScS* signals from the earthquake, respectively, and $\Delta T_k$ is the differential travel time between *S* and *ScS* at the $k$th station. Here we assume that *S* and *ScS* waveforms do not change much for a small regional array (with aperture of a few hundred kilometres), which is reasonable as the ray parameters and azimuth of *S* and *ScS* rays are almost same in such case. To alleviate probable effects of variable amplitude, we normalize each trace before applying our algorithm.

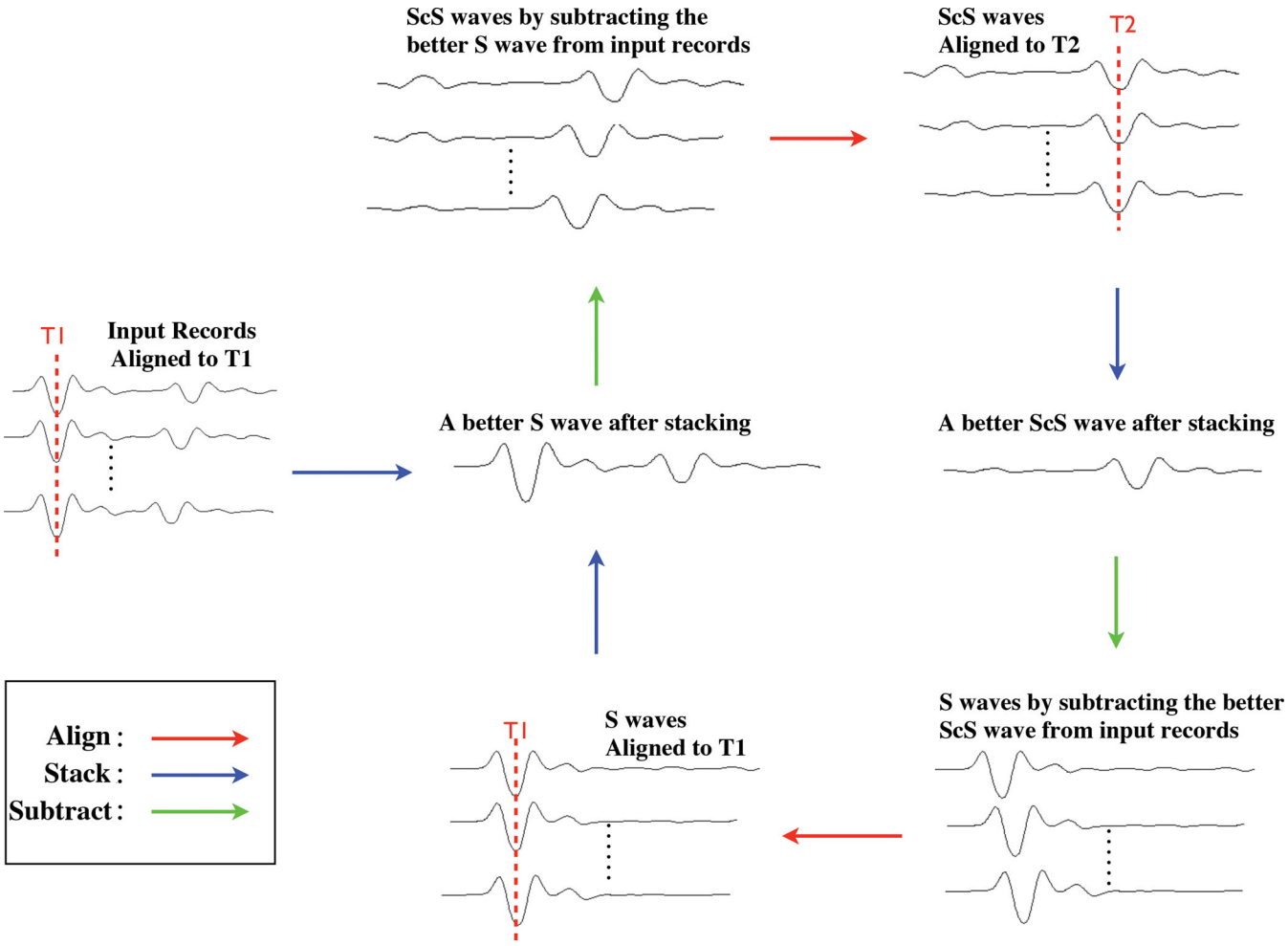


**Figure 2.** Flow chart of the algorithm showing how *S* and *ScS* are estimated iteratively.

The algorithm works in a straightforward and iterative way. We first enhance *S* wave by stacking waveforms aligned on *S* arrivals, then subtract *S* wave from each trace and enhance *ScS* by stacking the processed waveforms on *ScS* arrivals. Then *ScS* is removed from the original traces and better *S* can be estimated, after which better *ScS* waveform can be estimated by stacking the waveforms with better *S* wave subtracted. The procedure is iterated until no more improvements can be achieved. The iterative algorithm runs in this way with flow chart demonstrated in Fig. 2:

Initially set $S_{ScS}(t) = 0$

Step 1:
  Align each trace on *S* arrivals
  For each $k$
    Shift $S_{ScS}(t)$ by $\Delta T_k$ as predicted from theoretical *S*–*ScS* interval
    $X_k(t) = X_k(t) - S_{ScS}(t)$ (try to remove *ScS* from each $X_k(t)$)
  End
  $S_S(t) =$ average of $X_k(t)$ (obtain better estimate of *S*)

Step 2:
  For each $k$
    $X_k(t) = X_k(t) - S_S(t)$ (try to remove *S* from each $X_k(t)$)
  End
  Align each $X_k(t)$ on *ScS* arrivals
  $S_{ScS}(t) =$ average of $X_k(t)$ (obtain better estimate of *ScS*)
Go to step 1 for iteration.

To demonstrate effectiveness of the signal separation algorithm, we first apply it to three data sets of synthetic seismograms comprising of *S* and *ScS*, and compare recovered *S* and *ScS* waveforms with input ones to assess the accuracy.

Synthetic data set I contains 24 traces of seismograms constructed with *S* waves arriving on 0th s, and *ScS* waves arriving incrementally delayed from 4th to 50th s. That is, for the first trace, *ScS* is 4 s later than *S*, and for the second trace, *ScS* is delayed 2 more seconds, and so on. Therefore, for the 24th trace, *ScS* is delayed by 4 s + (24–1)*2s = 50 s. For each trace, the amplitude of *S* are constant and amplitude of *ScS* is set to be 1/3 of *S*, which is an ideal simplification of realistic seismic data. The *S* waveform is taken from a segment of observed tangential *SH* waveforms recorded at one of the GRSN stations from an aftershock of the Wenchuan earthquake, and is referred to as "source wavelet" (Fig. 3a). And *ScS* waveform is taken to be the same as *S* waveform. This data set forms the simplest time-series for validating our algorithm of *S* + *ScS* waveform separation because arrival, shape and amplitude of *S* and *ScS* are exactly known. A typical result is shown in Fig. 3(b). Only three traces are used in this test, and the comparison between the red line and black line in Fig. 3(b) suggests that the result completely matches the source wavelet.

Synthetic data set II contains seismograms at distances from 70° to 78°, computed with SEM (Spectral-element Method) for a point source (Komatitsch *et al.* 2002). SEM has the advantages of

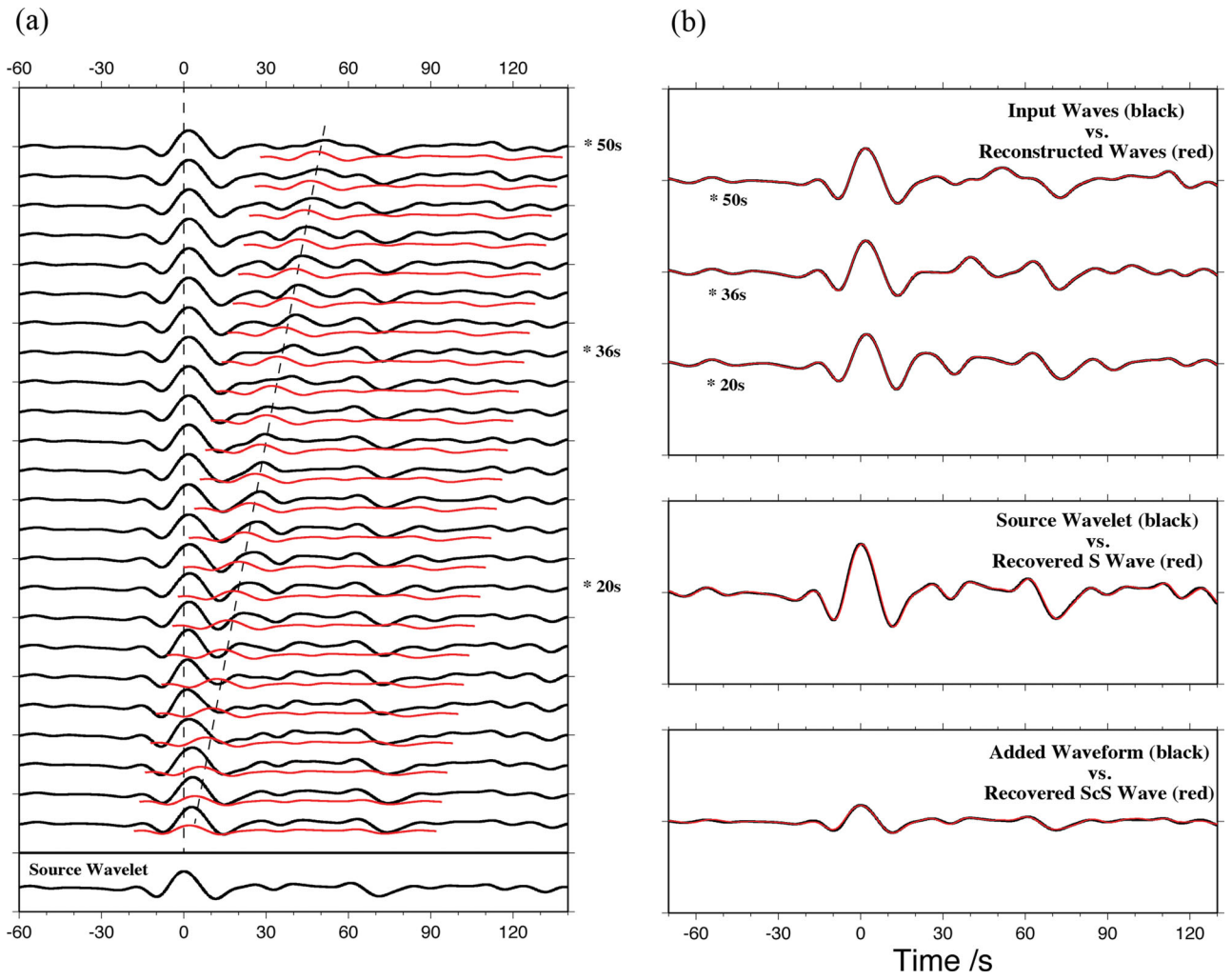


**Figure 3.** (a) Synthetic seismograms (black) constructed by combining a source wavelet aligned on 0th s to simulate *S* wave and a delayed source wavelet (red traces) to simulate *ScS* wave. (b) The top three traces are raw seismograms indicated by *20 s, *36 s and *50 s in 2a and reconstructed waveforms by combining recovered *S* (the fourth trace) and *ScS* (the fifth trace).

flexibility of grid meshing and robustness for velocity models featuring large contrasts. Moreover, SEM suffers of little numerical dispersion (Komatitsch *et al.* 2002). The velocity model used in constructing synthetic tangential seismograms is PREM, and the computation is performed in cylindrical grids of 1-D layered structure. For 1-D PREM model, theoretical arrivals of *S* and *ScS* can be computed straightforwardly. This data set is adopted to simulate more realistic seismograms because *S* and *ScS* do not necessarily keep identical waveform and amplitude over distances now. In Fig. 4, the result of applying the algorithm to two traces in this data set is shown to prove its benefit and correctness of iteration. After five iterations, the mismatch of the original record and reconstructed waveform of *S* and *ScS* waves shows obvious reduction. The recovered *S* and *ScS* waveforms agree with input ones well, as is shown in Figs 4(c) and (d). The test with five traces in this data set is shown in Fig. 5(a). Note the comparison of original waveforms and both reconstructed and recovered ones, they match each other quite well, which means the algorithm achieves our purpose to get the respective *S* and *ScS* waves accurately. To explore what effects of other seismic phases may have on robustness of our algorithm, we add a third phase into the previous five traces of SEM synthetics. The third phase is deliberately designed to be as strong as the *ScS* waves (Fig. 5d). The test suggests that with more than four records, the third phase could be obviously suppressed.

Synthetic data set III (Fig. 6a) consists of waveforms computed for a finite fault rupture model. The finite fault model (Fig. 6b) contains three asperities with hypocentre located in the asperity of largest slip with thrust mechanism. The second asperity features both strike slip and thrust components, while the third asperity only contains strike slip components. The rupture lasts 70 s. Strike and dip of the fault plane are 231° and 35°, respectively, as adopted from GCMT solution for the Wenchuan earthquake. We calculate the *SH* synthetics at teleseismic distances which form synthetic data set III. Here we use two kinds of Green's functions. One is calculated by the frequency-wavenumber integration method (Zhu & Rivera 2002) and another by a simplified ray theory code (Langston & Helmberger 1975). Compared with the first method, core phases (i.e. *ScS*, *sScS*, *PcP*, *sPcP*...) and multiple phases (i.e. *PP*, *PPP*, *SS*, *SSS*...) are not computed in the ray code. This data set is adopted to simulate even more realistic data because finite faulting and azimuthal effects are taken into account. Fig. 6 shows the results of a five-traces separation and a 10-traces separation. The recovered *S* waves are compared with the theoretical synthetics from the ray method. Due to the two methods' differences (FK synthetics have

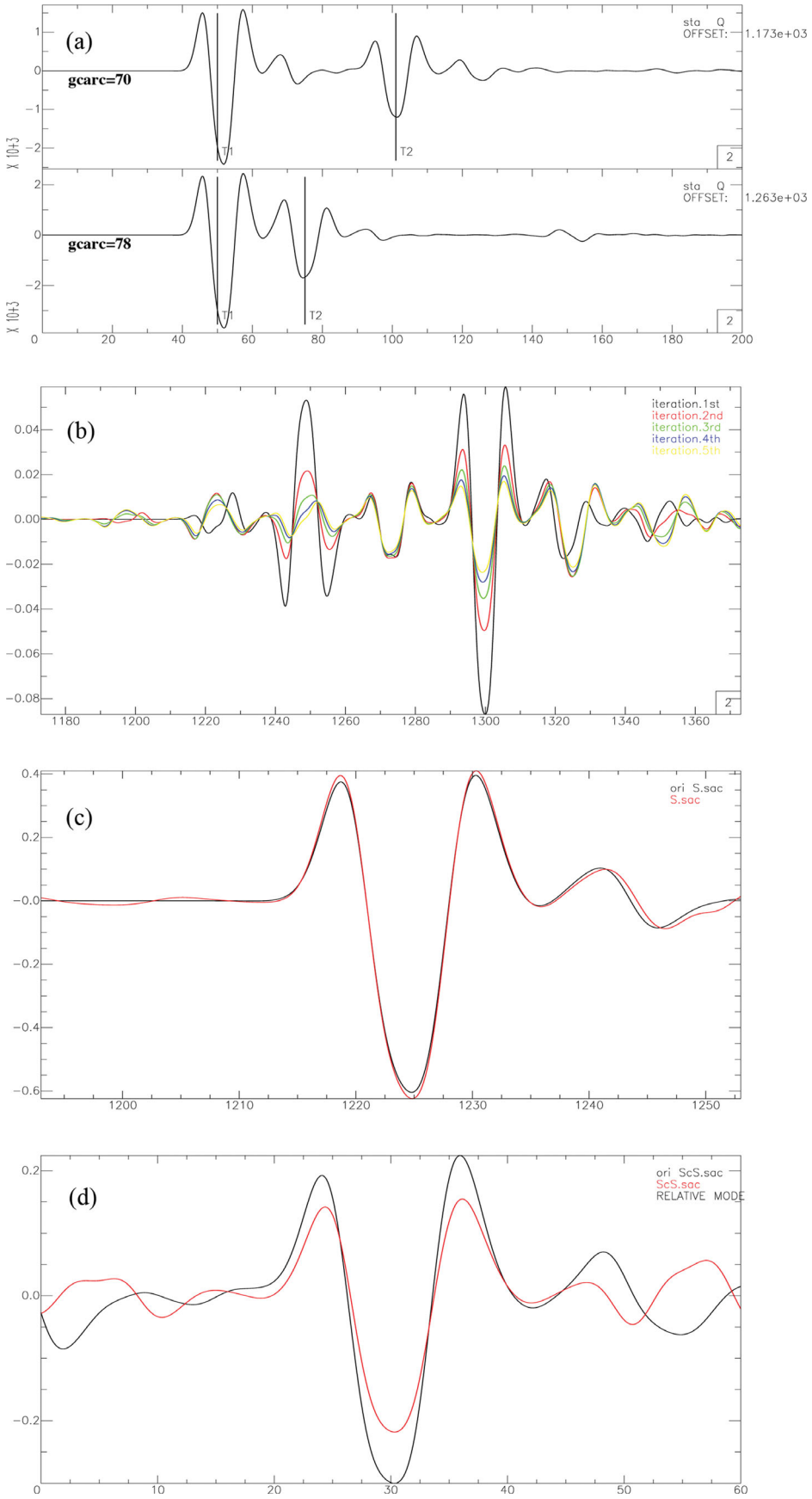


**Figure 4.** (a) Two traces of seismograms at 70° and 78° computed with SEM. (b) Evolution of residual (subtract recovered *S* and *ScS* from original trace at 70°) for each iteration. (c) Comparison between recovered *S* (red) and original *S* (black). (d) Same as (c), but for *ScS*.

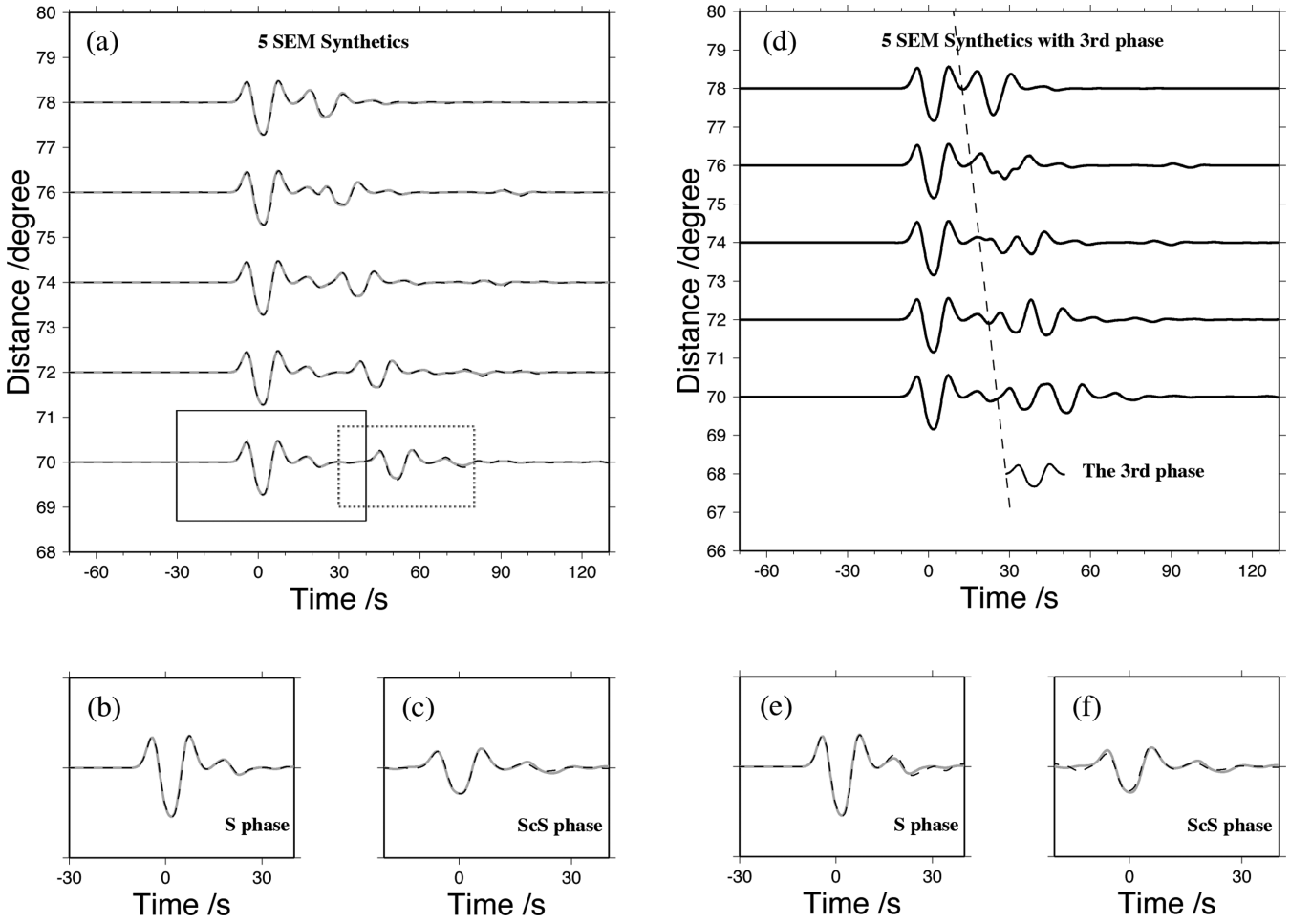


**Figure 5.** (a) Comparison between raw (grey) and reconstructed seimsograms (dashed). (b) Original (grey) and recovered *S* (dashed). (c) Original (grey) and recovered *ScS* (dashed). (d) A new set of five traces comprising of *S*, *ScS* and a third phase with arrival indicated with dashed line. (e) Same as (b) for wave separation on data in (d). (f) Same as (c) for wave separation on data in (d).

more phases than *S* and *ScS*, and use *Q* as the attenuation), the theoretical *S* phases of the two kinds of synthetics would be a bit different, which could be observed with the simplified *S* waveforms shown in Fig. 6(d). Therefore, with this factor taken into account, our separation provides reasonable and reliable recovered *S* waveform.

## APPLICATIONS

The above tests demonstrate that the *S* and *ScS* waveform recovery technique works for synthetic seismograms. Here we show that the algorithm also works for real data where *ScS* and *S* are well separated for the case of moderate earthquakes and where *ScS* and *S* overlap for the case of strong earthquakes. Unlike synthetic waveforms, the alignment of *S* or *ScS* is not straightforward. Because of 3-D heterogeneity, the traveltime of *S* or *ScS* can be substantially different from predictions based on 1-D Earth models (Ritsema *et al.* 1998; Ni & Helmberger 2003a). We adopt waveform cross correlation method in aligning *S* waveforms for moderate aftershocks, and the timing corrections can be applied to mainshock. With the approach, traveltime variability due to 3-D heterogeneity can be suppressed. Moreover, we lowpass filter observed *S* and *ScS* waveform, to avoid high variability of high frequency *SH* waveforms. Because of high attenuation of *S* waves in the mantle, high frequency *S* waves (4 s or shorter period) are weak, and microseisms are strong around 3–8 s. Therefore, we only model waveforms of period 10 s and longer.

As an $M_w$6.0 event, the 2008 August 5 aftershock of Wenchuan earthquake lasted for only a few seconds, much shorter than the differential time between *S* and *ScS* waves at distances around 70° (Fig. 7a). The record sections shows tangential *SH* waves aligned on *S* arrivals, and *ScS* is coherent and easy to be identified, implying that *ScS* can contaminate *S* wave if source duration is long enough. Recovered *S* and *ScS* are displayed as the bottom two traces in Fig. 7(a). To demonstrate that *ScS* wave has been successfully recovered, we subtract *ScS* waveform from each trace. We find that only signals with arrivals on *S* survives (Fig. 7b), and do not observe coherent signals near *ScS* arrivals. Similarly, we subtract *S* waveform from each trace (Fig. 7c), and obviously there are no coherent signals near *S* arrivals.

Then we process 22 *SH* waves of the $M_w$7.9 Wenchuan earthquake recorded at GRSN, whose *S* phases are overlapped by the *ScS* phases as discussed earlier. Fig. 7(d) is the separation result. It is obvious that the recovered *S* phase is quite different from the raw signals on each trace, arguing that the waves in the raw seismograms are not pure *S* waves. To show that *ScS* indeed contaminates *S* waves, we subtract *ScS* from raw traces (Fig. 7e). We find that the remaining signals are coherent at different distances and aligned well on *S*

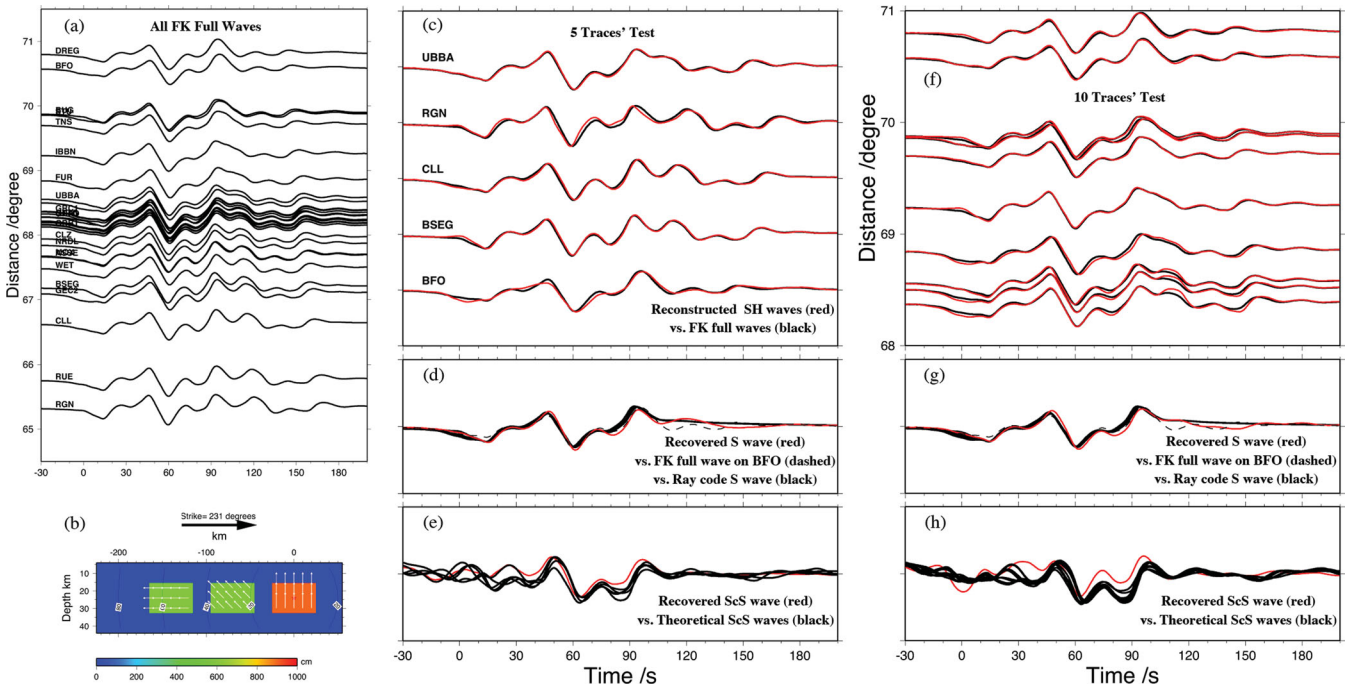


**Figure 6.** (a) FK synthetic tangential seismograms for a finite fault model. (b) the finite fault model consists of three asperities and the rupture duration is 70 s. (c) Raw (black) and reconstructed (red) seismograms for separation on five traces. (d) Comparison between recovered *S* (red), theoretical *S* waves computed with ray code (black) and Full synthetic wave train computed with FK (dashed). (e) Recovered *ScS* (red) and theoretical *ScS* (black) computed by removing ray code-computed *S* wave from full wave train computed with FK. The theoretical *ScS* waveform is computed in the above way because we do not have a code to compute *ScS* waves for finite fault models yet. (f,g,h) Same as (c,d,e) but for 10 traces.

arrivals, therefore they should be genuine *S* waves. With *ScS* contamination removed, we observe that the *S* waves last about 110 s, which can be translated to rupture duration around 110 seconds because the seismic rays to GRSN is perpendicular to rupture faults of the earthquake. *ScS* waveform differ from *S* probably due to different take angle angles of *ScS* and *S* ray paths which may cause different waveform for complicated earthquake slip models. The difference in *S* and *ScS* waveforms may thus provides more constraints on the rupture processes. Alternatively, *ScS* may be complicated by strong lateral variation in the D″ layer, for example, the Scd phase (Lay & Helmberger 1983). But from the results of the August 5 aftershock (Figs 7a–c), *ScS* is simple, implying that Scd is probably not strong.

But it is typically not realistic to have dozens of stations available for recovering *S* waves from seismograms contaminated by *ScS*. We investigate whether a few stations are sufficient for a successful recover of *S* waves. We test such possibility on waveform data at four stations with epicentral distance gap about 5° and azimuthal difference about 7°. The recovered *S* waveform from those four stations agrees well with that from 22 stations (Fig. 8), therefore it seems that four stations are effective in *S* and *ScS* separation.

## CONCLUSION AND DISCUSSION

For great earthquakes, *ScS* waves could interfere with *S* waves. To retrieve pure *S* component, we propose an effective, straightforward iterative algorithm to separate *S* and *ScS* phases from seismic traces recorded on a regional network. Compared with linear stacking, our algorithm works well while there are only 4–5 records available. Even when a third phase is present, the algorithm still produces reliable retrieval of *S* and *ScS*. However, the algorithm relies on two assumptions: (1) the two phases to be recovered of different distances should have similar shape and amplitude. (2) the differential time between *S* and *ScS* is well predicted by earth models. Assumption 1 is probably valid because the ray parameters of *S* and *ScS* are almost constant over a regional network. To investigate whether assumption (2) is valid for our study, we measure differential time between *S* and *ScS* for the *M*6 aftershock. It is found that the differential time is close to predictions based on IASP91 model (Fig. S1), and the observed differential time is only off up to 1.5 s from predictions, but the standard deviation is only about 0.7 s. Such minor variation of differential time has little effects on *S* and *ScS* waveform recovery as demonstrated in Fig. S2. In this figure, we change arrival of *ScS* randomly with time variation up to 1.5 s, and we do not observe much degradation of waveform recovery quality. But assumption (2) is not necessarily valid for regions of rapid and substantial shear velocity variation in the lowermost mantle (Ritsema *et al.* 1998; Ni & Helmberger 2003a,b; To *et al.* 2005). In this case, the alignment of *ScS* for the mainshock should be based on differential time of *S* and *ScS* measured from its aftershocks to account for rapid lateral variation of mantle structure.

Applications of the algorithm to the 2008 Wenchuan earthquake confirm that the substantial influence of the *ScS* energy makes the *S* wave trains last longer than rupture duration. As an important factor in finite fault inversion, the contaminated *S* waves will lead to an inaccurate rupture model. So, to achieve a better inversion, it is recommended to adopt our algorithm to get the clean *S* waves.

Traditionally, teleseismic *P* and *SH* waveforms are used to constrain the rupture process of great earthquakes. Ideally all the

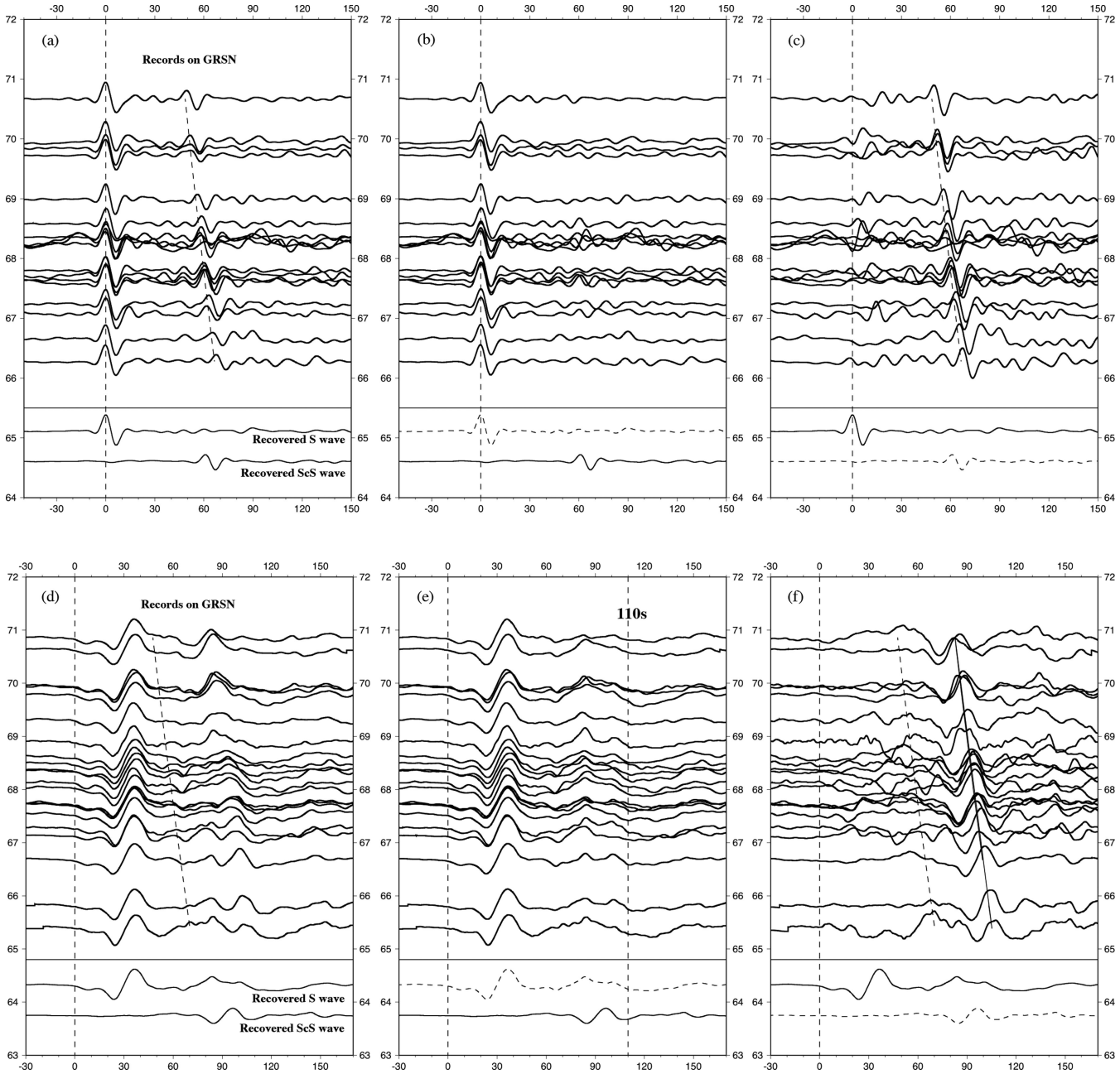


**Figure 7.** (a) Record section of tangential component seismograms of an aftershock of the Wenchuan earthquake recorded at GRSN. Traces are aligned on *S* arrivals. *ScS* is coherent, with arrival time well predicted with PREM. The bottom two traces are recovered *S* and *ScS* from the above traces. (b) Raw data with *ScS* removed. The traces are coherent and are very similar to recovered *S* wave (bottom dashed traces). (c) Raw data with *S* removed. (d,e,f) For the mainshock. Source duration is around 110 s as estimated from recovered *S* wave.

available data should be used for the inversion, but due to the computational costs and the redundancy of the data, usually only a subset of stations are chosen to have good azimuthal coverage. Most of the finite fault inversion methods adopt the simplified Green's function, ignoring the influence of the following phases (i.e. *ScS*). This is mainly because the timing incoherence between these phases on different stations with different epicentral distances, may average out the effect caused by the imperfect Green's function. And also the amplitude of these phases is assumed to be small. However, for some mechanisms, such as low angle mega-thrusts, the *ScS* amplitude is comparable with the direct *S* waves in some azimuthal ranges as demonstrated in this work. Thus, to reduce the artefact caused by these following phases, we should either include them in the Green's function or separate them before the records are used in the inversion.

## ACKNOWLEDGMENT

Waveform data is downloaded from IRIS and GRSN. We are grateful that Komatitsch provides SEM code. Supported by NSFC 40821160549, 41074032.

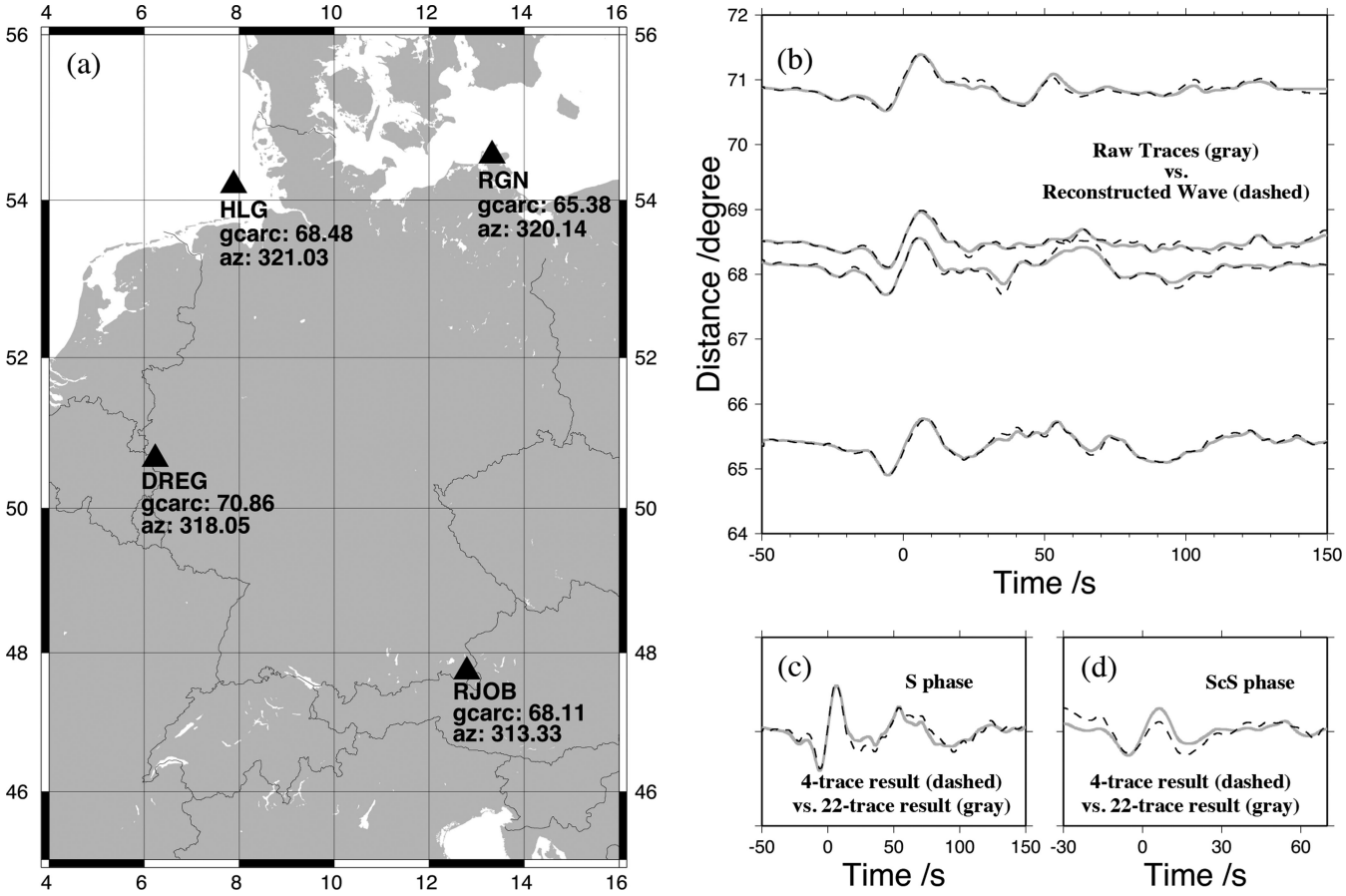


**Figure 8.** (a) Four stations (triangles) chosen for wave separation. (b) Comparison between raw data (grey) and reconstructed seismograms (dashed). (c) Comparison of recovered *S* from four traces (dashed) and that from 22 traces (grey). (d) Same as (c), but for *ScS* waves.

## REFERENCES


Ammon C. *et al*., 2005. Rupture process of the 2004 Sumatra-Andaman Earthquake, *Science,* **308,** 1133–1139.

Ammon, C.J., Lay, T., Kanamori, H. & Cleveland, M., 2011. A rupture model of the great 2011 Tohoku earthquake, *Earth planet. Space,* **20,** 1–4.

Antolik, M., Abercrombie, R.E., Pan, J. & Ekström, G., 2006. Rupture characteristics of the 2003 Mw 7.6 mid-indian Ocean earthquake: Implications for seismic properties of young oceanic lithosphere, *J. geophys. Res.*, **111,** B04302, doi:10.1029/2005JB003785.

Avants, M., Lay, T. & Garnero, E.J., 2006. A new probe of ULVZ S-wave velocity structure: array stacking of ScS waveforms, *Geophys. Res. Lett.,* **33,** L07314, doi:10.1029/2005GL024989.

Das, S. & Kostrov, B.V., 1990. Inversion for seismic slip rate history and distribution with stabilizing constraints: application to the 1986 Andrean of Islands earthquake, *J. geophys. Res.,* **95,** 6899–6913.

Fukuyama, E. & Mikumo, T., 1993. Dynamic rupture analysis: inversion for the source process of the 1990 Izu-Oshima, Japan, earthquake (M = 6.5), *J. geophys. Res.,* **98,** 6529–6542.

Hartzell, S.H. & Heaton, T.H., 1983. Inversion of strong ground motion and teleseismic waveform data for the fault rupture history of the 1979 Imperial Valley, California, earthquake, *Bull. seism. Soc. Am.,* **73,** 1553–1583.

Houston, H., 2001. Influence of depth, focal mechanism, and tectonic setting on the shape and duration of earthquake source time functions, *J. geophys. Res.,* **106,** 11 137–11 150.

Ishii, M., Shearer, P.M., Houston, H. & Vidale, J.E., 2005. Rupture extent, duration, and speed of the 2004 Sumatra-Andaman earthquake imaged by the Hi-Net array, *Nature*, **435,** 933–936.

Ji, C., Wald, D.J. & Helmberger, D.V., 2002. Source description of the 1999 Hector Mine, California, earthquake, Part I: wavelet domain inversion theory and resolution analysis, *Bull. seism. Soc. Am.,* **92,** 1192–1207.

Kanamori, H. & Anderson, D.L., 1975. Theoretical basis of some empirical relations in seismology, *Bull. seism. Soc. Am.,* **65,** 1073–1095.

Kikuchi, M. & Kanamori, H., 1982. Inversion of complex body waves, *Bull. seism. Soc. Am.*, **72,** 491–506.

Komatitsch, D., Ritsema, J. & Tromp, J., 2002. The spectral-element method, Beowulf computing, and global seismology, *Science,* **298,** 1737–1742.

Kruger, F. & Ohrnberger, M., 2005. Tracking the rupture of the Mw = 9.3 Sumatra earthquake over 1,150 km at teleseismic distance, *Nature*, **435,** 937–939.

Langston, C.A. & Helmberger, D.V., 1975. Procedure for modeling shallow dislocation sources, *Geophys. J. R. astr. Soc.,* **42,** 117–130.

Lay, T. & Helmberger, D.V., 1983. A lower mantle S wave triplication and the shear velocity structure of DU, *Geophys. J. R. astr. Soc.,* **75,** 799–838.

Mendoza, C. & Hartzell, S.H., 1988. Inversion for slip distribution using teleseismic P waveforms: north Palm Springs, Borah Peak, and Michoacan earthquakes, *Bull. seism. Soc. Am.,* **78,** 1092–1111.

Ni, S. & Helmberger, D.V., 2003a. Ridge-like lower mantle structure beneath South Africa, *J. geophys. Res.,* **108,** 2094, doi:10.1029/2001JB001545.

Ni, S. & Helmberger, D.V., 2003b. Further constraints on the African superplume structure, *Phys. Earth planet. Inter.,* **140,** 243–251.

Ni, S., Kanamori, H. & Helmberger, D.V., 2005. Energy radiation from the Sumatra earthquake, *Nature,* **434,** 582, doi:10.1038/434582a.

Olson, A.H. & Apsel, R.J., 1982. Finite faults and inverse theory with applications to the 1979 Imperial Valley earthquake, *Bull. seism. Soc. Am.,* **72,** 1969–2001.

Peltzer, G. & Rosen, P., 1995. Surface displacement of the 17 May 1993 Eureka Valley, California, earthquake observed by SAR interferometry, *Science,* **268,** 1333–1336.

Pino, N.A., Mazza, S. & Boschi, E., 1999. Rupture directivity of the major shocks in the 1997 Umbria-Marche (central Italy) sequence from regional broadband waveforms, *Geophys. Res. Lett.,* **26,** 2101–2104.

Ritsema J., Ni, S. & Helmberger D.V., 1998. Evidence for strong shear velocity reductions and velocity gradients in the lower mantle beneath Africa, *Geophys. Res. Lett.,* **25,** 4245–4248.

Rondenay, S. & Fischer, K.M., 2003. Constraints on localized core-mantle boundary structure from multichannel, broadband SKS coda analysis, *J. geophys. Res.,* **108,** B11, doi:10.1029/2003JB002518.

Shen, Z.K. *et al*., 2009. Slip maxima at fault junctions and rupturing of barriers during the 2008 Wenchuan earthquake, *Nat. Geosci.,* **2,** 718–724.

Simons, M. *et al*., 2011. The 2011 Magnitude 9.0 Tohoku-Oki earthquake: mosaicking the megathrust from seconds to centuries, *Science,* **332,** 1421–1425.

To, A., Romanowicz, B., Capdeville, Y. & Takeuchi, N., 2005. 3D effects of sharp boundaries at the borders of the African and Pacific Superplumes: observation and modeling, *Earth planet. Sci. Lett.,* **233,** 137–153.

Xu, Y., Koper, K.D., Sufri, O., Zhu, L. & Hutko, A.R., 2009. Rupture imaging of the Mw 7.9 12 May 2008 Wenchuan earthquake from back projection of teleseismic P waves, *Geochem. Geophys. Geosyst.,* **10,** Q04006, doi:10.1029/2008GC002335.

Zhang, W., Shen, Y. & Chen, X., 2008. Numerical simulation of strong ground motion for the Ms8.0 Wenchuan earthquake of 12 May 2008, *Sci. China Ser. D-Earth Sci.,* **51,** 1673–1682.

Zhu, L. & Rivera, L.A., 2002. A note on the dynamic and static displacements from a point source in multi-layered media, *Geophys. J. Int.,* **148,** 619–627.

## SUPPORTING INFORMATION

Additional Supporting Information may be found in the online version of this article:

**Figure S1.** Differential time of *S* and *ScS* with respect to IASP91 prediction for the waveform data recorded on GRSN from the *M*6 aftershock.

**Figure S2.** Effects of differential time between *S* and *ScS* on waveform recovery quality. (a) same as Fig. 3, the test of synthetic data set I, recovered *S*, *ScS* (three times amplitude) waveforms and the source wavelet are figured together in different colour for comparison. (b)–(d) the differential time is disturbed randomly within range of 1.5 s. The values next to each trace show the traveltime shift.

Please note: Wiley-Blackwell are not responsible for the content or functionality of any supporting materials supplied by the authors. Any queries (other than missing material) should be directed to the corresponding author for the article.